ACS APPLIED MATERIALS & INTERFACES

www.acsami.org

Research Article

Universal Coating Strategy Breaks Stability-Performance Trade-Off in Macroscopic Graphene Films

Mingyang Tanwei,[⊥] Zibo Chen,[⊥] Yunfa Si, Yongyi Ji, Shiya Cao, Zhenyu Gong, Bao-Wen Li, Bo Liu,* Geng Wu,* and Daping He*

Cite This: https://doi.org/10.1021/acsami.5c05545

Read Online

ACCESS | Metrics & More | Article Recommendations | Supporting Information

ABSTRACT: Macroscopic graphene film (MGF), excelling in superior electric and thermal conductivities, holds great promise in energy storage, thermal management, and flexible electronics. However, the high graphitization of MGF leads to surface fragility because of the weak interlayer interaction, leading to severe performance limitations. Herein, we report an interface engineering strategy for the thinnest coating on MGF to date, significantly enhancing surface stability while preserving ultrahigh electric and thermal conductivities. With a surfactant-enhanced interface self-assembly strategy, we construct a 5 nm thick Triton X-100-enhanced graphene oxide coating on MGF (MGF@TGO). This modification increases the surface adhesion by 206.36% while maintaining over 99% of its electrical and thermal conductivities. MGF@TGO serves as an effective thermal management unit, exhibiting excellent stability without surface detachment under simulated operating conditions. Depth profiling characterizations reveal that hydrogen bonding and $\pi-\pi$ stacking costrengthen the MGF@TGO surface. Notably, our strategy is universally applicable to multiple aromatic-polar amphiphilic surfactants. This work successfully balances surface stability with performance retention, offering a scalable solution for MGF applications in industry.

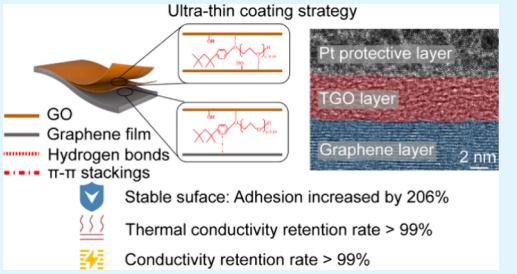

KEYWORDS: *macroscopic graphene film, surfactant-enhanced interface self-assembly strategy, surface stability*

Downloaded via WUHAN UNIV OF TECHNOLOGY on June 12, 2025 at 08:33:00 (UTC).
See https://pubs.acs.org/sharingguidelines for options on how to legitimately share published articles.

INTRODUCTION

Macroscopic graphene film (MGF), enabling transmitting superior electric and thermal conductivities from 2D graphene nanosheets to the macroscopic scale, has been broadly applied in energy storage,[1−3] thermal management,[4−6] and flexible electronics.[7−10] Recently, Li et al. have used MGF as collectors to replace traditional Cu/Al foils and effectively restrained the thermal runaway of Li-ion batteries.[11] Lee et al. use ultrathin Au/graphene hybrid films to modify thermal emissivity, providing a versatile solution for thermal management applications.[12] Although MGF can be manufactured through multiple methods,[13−15] the graphitization for carbon repairing at high temperatures is inevitable to obtain MGF with ultrahigh electric and thermal conductivities. This leads to the leap of aromaticity, leaves domination of $\pi-\pi$ stacking among nanosheets, and causes fragility on the surface (Figure 1a). Specifically, a negative stiffness region appears between the outermost and suboutermost layers when an external force is applied to MGF, causing slips and an unstable surface (Figure 1b).[16−19] This structure failure may further cause severe consequences in applications, including electrode material falling off during the cycle, graphene fragments falling off, and causing circuit short circuits.

To enhance the stability of the MGF surface, two mainstream strategies have arisen but still face multiple challenges. Internal reinforcement cross-linking strengthens the interaction between graphene nanosheets but requires complex technologies to intercalate into it, with a large deterioration in electrical and thermal conductivities of MGF.[20−22] Due to the surface vulnerability, external reinforcement coating enhances the stability of the surface while maintaining the original structure of MGF. However, tradi-

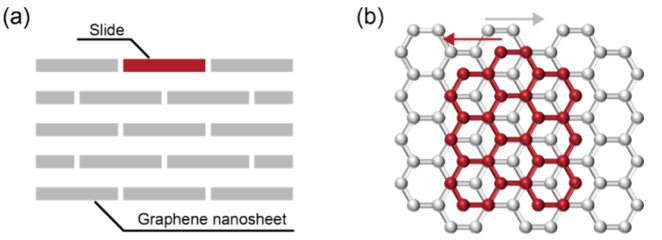

Figure 1. Schematic diagram of the MGF surface detachment. (a) Schematic diagram of MGF surface sliding (side view). (b) Schematic diagram of MGF surface sliding (top view).

Received: March 19, 2025
Revised: June 2, 2025
Accepted: June 4, 2025

© XXXX American Chemical Society

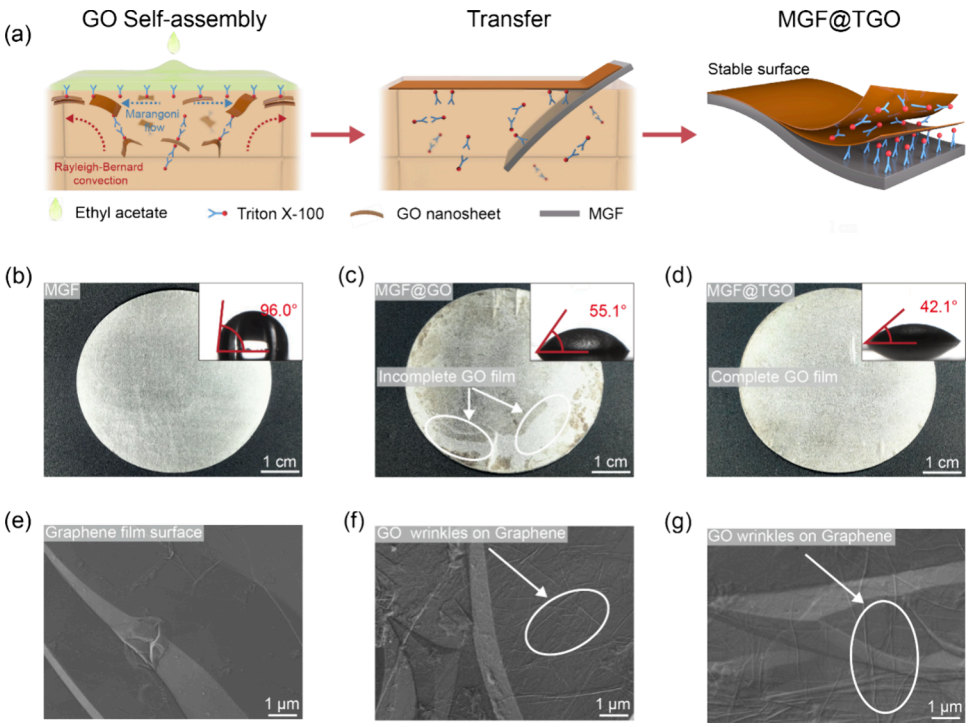

Figure 2. Fabrication of the SIS strategy. (a) Fabrication schematic of MGF@TGO. (b–d) Optical photographs and contact angle (inset) of MGF (b), MGF@GO (c), and MGF@TGO (d). (e–g) SEM images MGF (e), MGF@GO (f), and MGF@TGO (g).

tional coatings (usually submicron to micron thickness) generate more than 10% loss in electric and thermal conductivities when applied on the MGF surface.[23−26] Constructing ultrathin and stable coating, enabling electron tunneling[27] and phonons' ballistic transport[28] given by size effects, is a key breakthrough in overcoming the "stability-performance" balance. Graphene oxide, a potential 2D material, is capable of forming ultrathin and even coatings.[29−34] However, its strong polarity is incompatible with aromatic MGF, resulting in the interface bonding strength of GO coatings failing to meet actual working requirements.

In this work, we present an interface engineering method for the thinnest coating to date on MGF, enhancing surface stability while preserving ultrahigh electric and thermal conductivities. Using a surfactant-enhanced interface self-assembly (SIS) strategy, we successfully constructed a 5 nm thick Triton X-100 (Triton)-enhanced GO coating on MGF (MGF@TGO). This coating effectively mitigates the surface detachment of MGF, with the enhancement of surface adhesion of MGF@TGO by 206.36%. Through C K-edge X-ray absorption near edge structure (XANES) and depth profiling X-ray photoelectron spectroscopy (XPS) characterization, we confirm that Triton enhances the mechanical properties of the coating via hydrogen bonding and strengthens the adhesion between the coating and MGF through $\pi-\pi$ stacking interactions. Moreover, we discovered that multiple aromatic-polar amphiphilic surfactants can also form ultrathin, robust GO coatings under the SIS strategy. Benefiting from the ultrathin coating, MGF@TGO retains over 99% of its electric conductivity along with in-plane and through-plane thermal conductivity at the device level (an order-of-magnitude advantage over current methods). We demonstrate MGF@TGO as thermal management devices, exhibiting excellent performance without surface detachment. Our work successfully resolves the longstanding conflict between surface stability and properties maintained for MGF, thereby providing a compelling solution and immediate possibilities for the MGF industry.

RESULTS AND DISCUSSION

Preparation of MGF@TGO by the SIS Strategy. We fabricated ultrathin TGO coatings via self-assembly (Figure 2a). Triton is first incorporated into the GO solution and subjected to thorough dispersion. Next, ethyl acetate (EA) is added to the TGO dispersion prepared in deionized water. Due to its limited solubility and lighter density, EA forms a separate liquid layer atop the solution. The high vapor pressure and low boiling point of EA promote its rapid evaporation, which induces Marangoni flow and Rayleigh–Bénard convection within the system. These dynamic effects facilitate the self-assembly of TGO sheets into a coherent coating at the solution's surface.[35−38] Within a short time, complete evaporation of EA yielded the final ultrathin TGO coatings (Figure S1). Notably, a large-sized GO (Figure S2) is employed to fabricate the TGO coating, ensuring both uniformity and high assembly effectiveness (Figure S3). The resultant TGO coating is then transferred onto MGF (Figure S4), and following a vacuum drying process, a MGF@TGO film is obtained. An analogous procedure is employed to prepare MGF@GO.

From a macroscopic perspective, pristine MGF (Figure 2b) exhibits a silvery-white luster. Additionally, MGF shows a water contact angle of 96.0°, a strong (002) peak at $2\theta = 26.5°$ in the X-ray diffraction (XRD) pattern, and a sharp G band at 1580 cm^{-1} in the Raman spectrum (Figures S5 and S6), these features indicate MGF's high graphitization.[39,40] In contrast, the surfaces of MGF@GO (Figure 2c) and MGF@TGO (Figure 2d) appear light-yellow, confirming the successful wrapping of GO on MGF. Furthermore, a complete and more uniform TGO coating on MGF@TGO compared to the GO

https://doi.org/10.1021/acsami.5c05545
ACS Appl. Mater. Interfaces XXXX, XXX, XXX−XXX

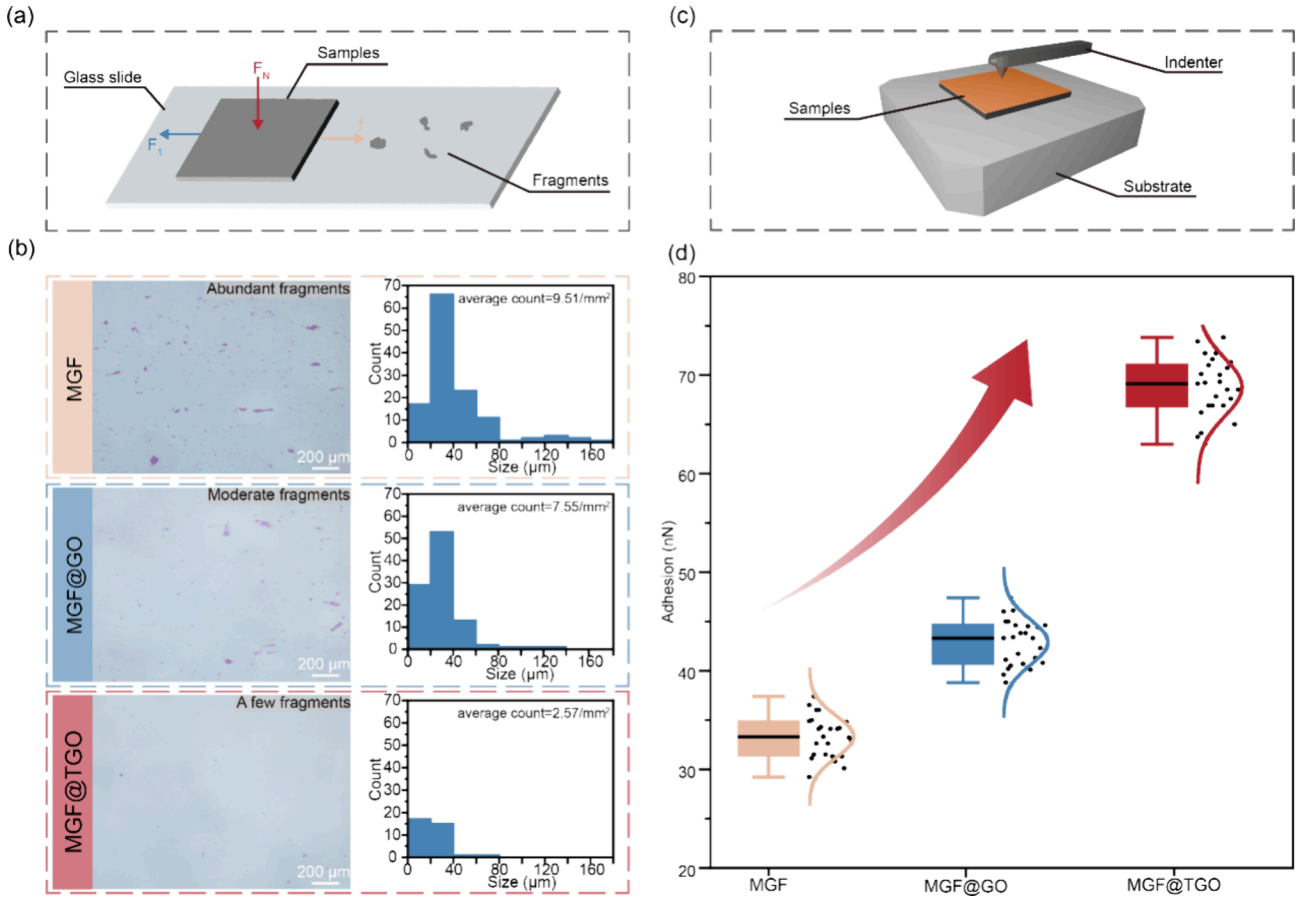

Figure 3. Friction and adhesion testing of different samples. (a) Schematic diagram of friction test. (b) Optical images and statistics of detached fragments of different samples on glass slides. (c) Schematic diagram of AFM for adhesion testing. (d) Box plots of adhesion for different samples (25 points for each sample).

coating on MGF@GO demonstrates that Triton enhances the compatibility between GO and graphene. This result is also supported by the lower contact angle of 55.1° for MGF@GO, as GO exhibits hydrophilicity due to oxygen-containing functional groups, while the lowest angle (42.1°) of MGF@TGO likely arises from its flattest surface. Moreover, owing to the improved compatibility between GO and graphene, MGF@TGO demonstrates excellent stability in aqueous environments, with TGO remaining adhered to the MGF surface after 1 week of immersion in deionized water (Figure S7). Scanning electron microscopy (SEM) is conducted for microstructural analysis. Pristine MGF (Figure 2e) displays typical micrometer-sized wrinkles, while both MGF@GO (Figure 2f) and MGF@TGO (Figure 2g) exhibit additional nanoscale GO wrinkles superimposed on the original micrometer-sized wrinkles, indicating the ultrathin thickness and robust adhesion of the GO/TGO coatings.

Enhanced Surface Stability of MGF@TGO. To evaluate the surface stability of samples, we designed a friction experiment, as illustrated in Figure 3a. Constant pressure is applied to the sample on a glass slide for uniform friction subsequently. After testing, the glass slide is examined under an optical microscope, and the size and quantity of graphene fragments detached from an area of 13 mm^2 are statistically analyzed (Figure S8). Figure 3b shows the obtained results. Notably, fragments of MGF on slides are observed and measured, exceeding 100 μm in diameter. The surface of MGF is prone to wear (Figure S9) and detachment due to weak interlayer adhesion between graphene sheets. For MGF@GO, similar to MGF, a substantial number of graphene fragments detach due to insufficient interactions between GO and graphene. In contrast, MGF@TGO exhibits significantly improved stability, with optical microscopy revealing a dramatic reduction in the number of detached graphene fragments, and no large-sized fragments are observed.

To quantify the stability enhancement, an atomic force microscope (AFM) with external facilities (Figure 3c) is used to measure the adhesion force values among different samples, with detailed data provided in Figure S10. As shown in Figure 3d, MGF@TGO exhibits a strong adhesion force of 68.76 nN, which is 206.36% higher than that of MGF (33.32 nN) and significantly greater than that of MGF@GO (42.89 nN). This robust adhesion is critical for enhancing the surface stability of MGF@TGO. We attribute the enhanced stability of MGF@TGO to the interactions mediated by Triton between GO and graphene, which strengthen the adhesion between the two materials. However, the precise mechanism by which Triton improves the stability of the MGF@TGO requires further investigation.

Enhancement Mechanism of MGF@TGO. To evaluate the thickness of the TGO coating on the MGF@TGO surface and its interaction with MGF, we conduct cross-sectional high-resolution transmission electron microscopy (HRTEM) analysis with the samples prepared by ion beam milling at −150 °C (Figure S11). Figure 4a shows that the ultrathin TGO layer, approximately 5 nm thick, tightly adheres to the

https://doi.org/10.1021/acsami.5c05545
ACS Appl. Mater. Interfaces XXXX, XXX, XXX−XXX

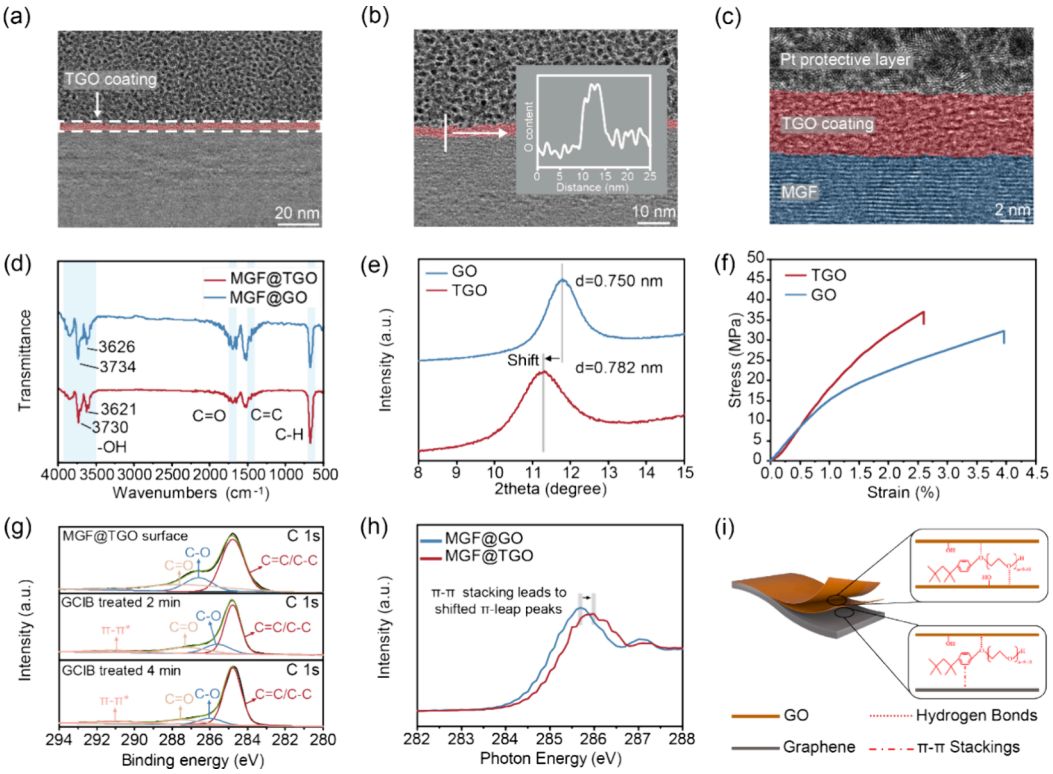

Figure 4. Mechanisms and characterization of SIS strategy (a) HRTEM cross-section image of MGF@TGO. (b) HRTEM cross-section EDS image of MGF@TGO. (c) HRTEM cross-section image at the interface of TGO and MGF. (d) FT-IR spectra of MGF@TGO and MGF@GO. (e) XRD pattern of TGO and GO. (f) Stress−strain curves of TGO and GO. (g) XPS spectra of the MGF@TGO surface after different GCIB treatment times. (h) C K-edge XANES of MGF@TGO and MGF@GO. (i) Schematic representation of the structure and interactions of MGF@TGO.

graphene surface. Raman spectroscopy reveals a significant enhancement of the D band in MGF@TGO compared to MGF (Figure S6), and HRTEM energy-dispersive spectroscopy (EDS) (Figure 4b) shows an increased oxygen content over a region approximately 5 nm in thickness, confirming the presence and ultrathin nature of the TGO layer. Further magnification (Figure 4c) clearly resolves the graphene lattice fringes of MGF and the amorphous structure of TGO, with the smooth TGO layer tightly adhering to the graphene surface. No gaps are observed at the interface, indicating a strong adhesion between TGO and graphene.

The stability of MGF@TGO requires a robust TGO coating, which in turn necessitates that TGO itself is strong and forms strong interactions with MGF. To explore the enhancement mechanism of Triton within TGO, Fourier transform infrared (FT-IR) spectroscopy is employed (Figure 4d). A split hydroxyl peak in the 3500−3850 cm^{-1} range is observed, a characteristic feature of ultrathin GO. Additionally, a redshift of the hydroxyl peak in MGF@TGO compared to MGF@GO indicates that Triton X-100 forms hydrogen bonds with GO, thus enhancing the interaction between GO layers. XRD is further used to investigate the interlayer changes in TGO. As shown in Figure 4e, the (001) peak of TGO shifts to a smaller angle orientation compared to GO, with the interlayer spacing of TGO increasing from 0.750 nm in GO to 0.782 nm in TGO, suggesting that Triton intercalates between the GO layers. Moreover, in scale-up tensile strength tests (Figure 4f), the slope of TGO is greater than that of GO, along with an expanded elastic strain range, indicating an increase in the Young's modulus of TGO, which demonstrates the enhancing effect of Triton on the mechanical properties of GO. Based on these results, we conclude that the formation of a tough TGO coating arises from the intercalation of Triton between GO nanosheets and the formation of hydrogen bonds, which enhance the intrinsic mechanical properties of TGO.

To explore the interaction between TGO and MGF, we performed XPS depth profiling (Figures 4g and S12). XPS analysis before Ar gas cluster ion beam (GCIB) treatment shows the presence of C=O and C−O, confirming the presence of TGO on the surface. After 2 min of GCIB treatment, the C=O and C−O content decreases significantly, and a $\pi-\pi$ satellite peak appears. After 4 min of treatment, the C=O and C−O content further decreases, and the intensity of the $\pi-\pi$ satellite peak increases (Figure S13), indicating that the MGF layer is etched. These results suggest that the sample treated for 2 min with GCIB is located at the TGO-MGF interface, and the $\pi-\pi$ satellite peak observed arises from the interaction between Triton and graphene. Moreover, in C K-edge XANES, the π leap in MGF@TGO shifts to higher energy and weakens compared to MGF@GO (Figure 4h), which is attributed to the formation of $\pi-\pi$ stacking between Triton and MGF in MGF@TGO.[41,42] Combining the data from XPS and XANES, it is proven that $\pi-\pi$ stacking exists at the TGO-MGF interface in MGF@TGO. In short, the excellent surface stability of MGF@TGO arises from the structure illustrated in Figure 4i. Within TGO, the cross-linking of Triton between GO nanosheets through hydrogen bonding enhances the tensile strength of TGO, resulting in the formation of a strong and tough TGO coating. TGO coating adheres tightly and robustly to the MGF surface through $\pi-\pi$

https://doi.org/10.1021/acsami.5c05545
ACS Appl. Mater. Interfaces XXXX, XXX, XXX−XXX

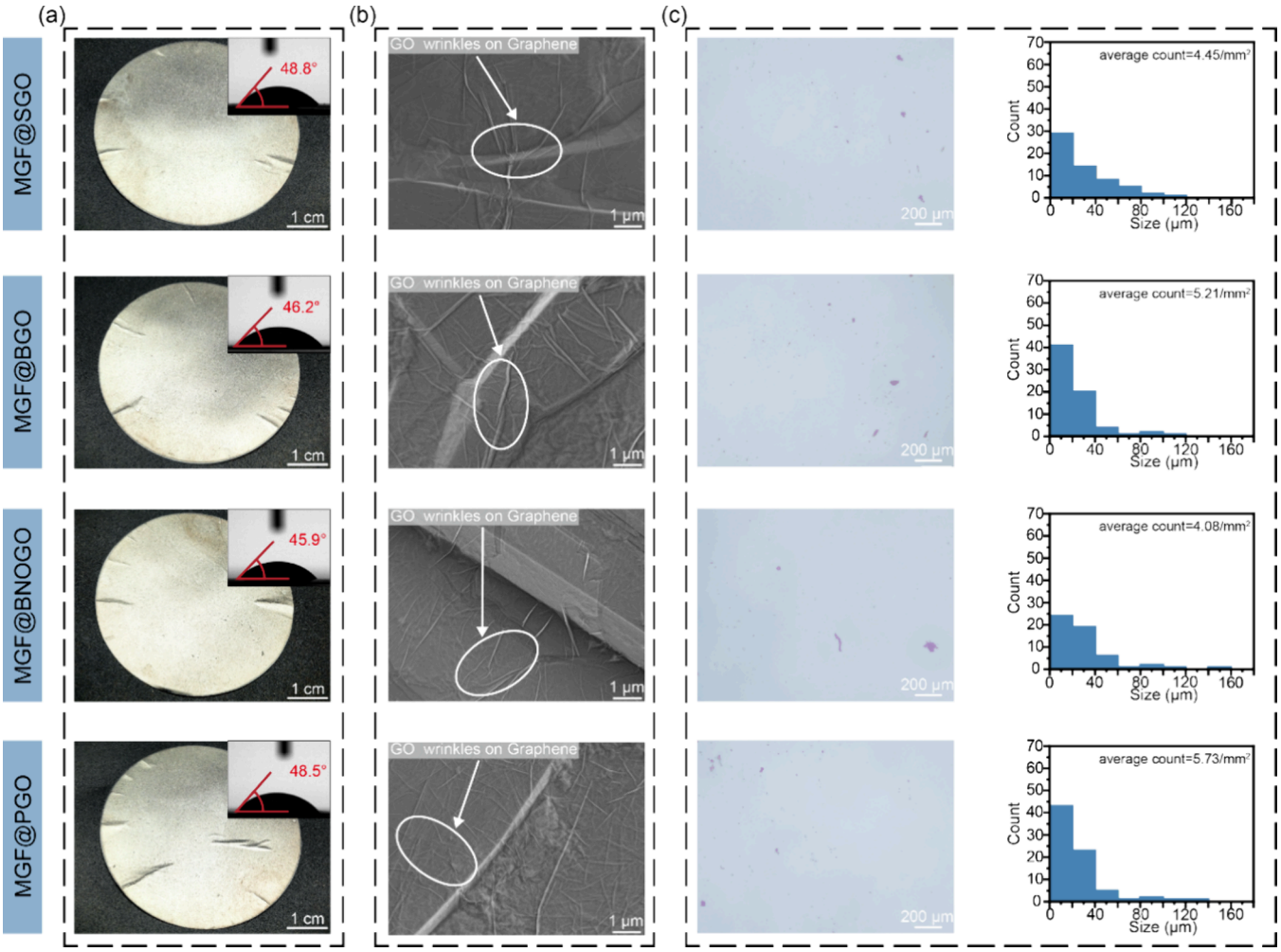

Figure 5. Universality of the SIS strategy. (a) Optical images and contact angle of different samples. (b) SEM images of different samples. (c) Optical images and statistics of detached fragments of different samples on glass slides.

stacking interactions mediated by Triton, which forms surface-stable MGF@TGO.

Universality of the SIS Strategy. Building upon the Triton-mediated enhancement mechanism for MGF@TGO, we systematically investigate four structurally similar surfactants that contain both aromatic and polar groups: sodium dodecylbenzenesulfonate (SDBS, anionic), benzalkonium chloride (BC, cationic), 2-naphthol polyoxyethylene ether (BNO12, nonionic), and diphenylphenol polyoxyethylene ether (PSPE, nonionic). Following the established MGF@TGO preparation protocol, we successfully synthesized SDBS, BC, BNO12, and PSPE-enhanced GO coatings on MGF, denoted as MGF@SGO, MGF@BGO, MGF@BNOGO, and MGF@PGO, respectively. Optical observations and contact angle measurements (Figure 5a) reveal that all four samples exhibit uniform light-yellow coloration and enhanced wettability, indicating uniform GO coating with high quality. SEM images further reveal the presence of a nanoscale wrinkled GO morphology on the MGF surface (Figure 5b). Notably, friction tests demonstrate a significant reduction in fragments shed compared to MGF@GO, confirming the effectiveness of amphiphilic surfactant enhancement (Figures 5c and S14). Furthermore, ionic surfactants show homogeneity with nonionic surfactants, including Triton, resulting from the low concentration of GO and surfactants to avoid aggregation. The SIS strategy, applied with the four surfactants, consistently reduces the amount of debris shed from the composite films, verifying the universality of the SIS strategy.

MGF@TGO for Applications. To evaluate the effect of the TGO coating on the intrinsic properties of MGF for applications, a series of tests is conducted. Figure 6a shows the white light interferometry image obtained by using an optical profilometer. The presence of the TGO coating reduces the roughness average (Ra) of MGF@TGO (0.687) compared to MGF (0.716), minimizing gaps between MGF and the heating device and thereby enhancing heat transfer efficiency. Moreover, MGF@TGO (1.32×10^6 S m^{-1}) maintains over 99% of the electrical conductivity of MGF (1.33×10^6 S m^{-1}) owing to the ultrathin nature of the TGO coating (Figure 6b). Furthermore, thermal conductivity measurements using the setup are shown in Figure S15 reveal that MGF@TGO retains thermal conductivities of 1412 W m^{-1} K^{-1} $\kappa_{\parallel}$ and 13.90 W m^{-1} K^{-1} $\kappa_{\perp}$, preserving over 99% of MGF's thermal performance (Figures 6c and S16). Additionally, benefiting from the reduced surface roughness, the interface thermal resistance of MGF@TGO under low pressure is significantly better than that of MGF, and a maximum optimization of 26.82% is achieved at 50 psi (Figure S17).

To measure the performance of MGF@TGO under operating conditions, we propose a simulation test for an

https://doi.org/10.1021/acsami.5c05545
ACS Appl. Mater. Interfaces XXXX, XXX, XXX−XXX

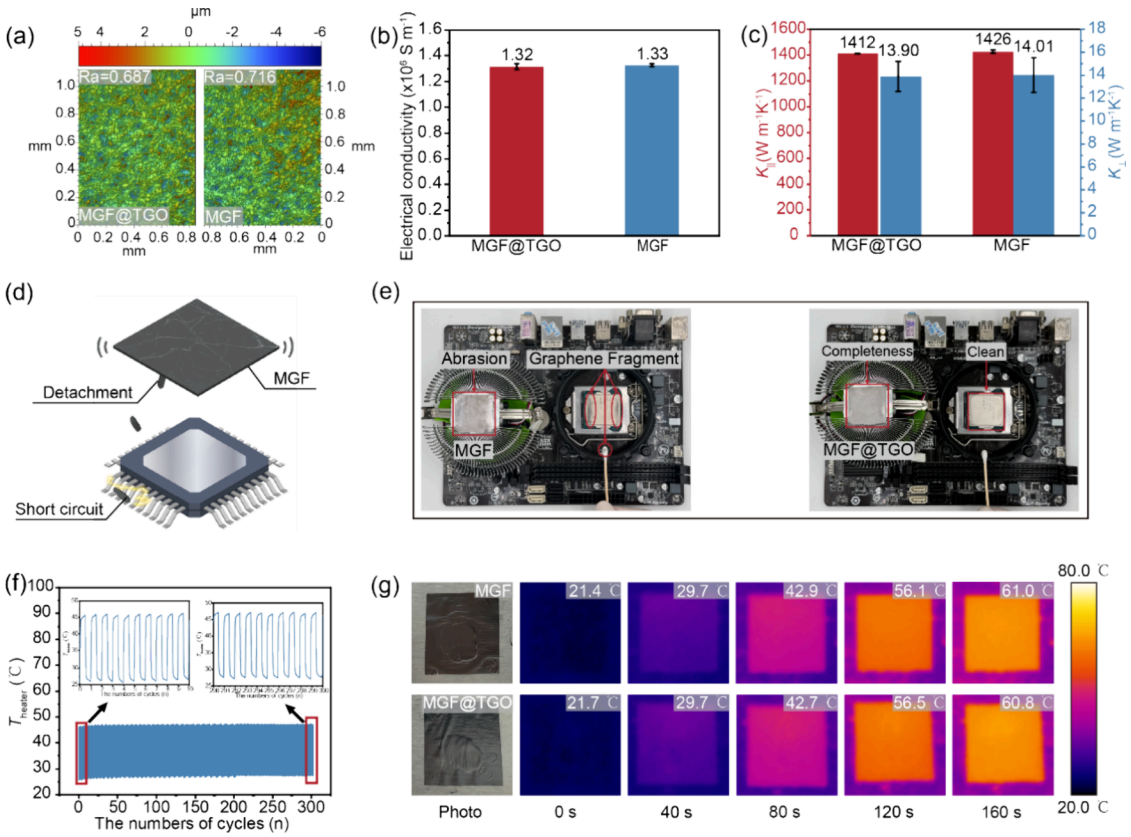

Figure 6. MGF@TGO was used for application. (a) Ra of MGF@TGO and MGF. (b) Electrical conductivity of MGF@TGO and MGF. (c) In-plane, through-plane thermal conductivity of MGF@TGO and MGF. (d) Schematic diagram of fragment detachment in MGF application. (e) Photos of MGF and MGF@TGO in operating conditions. (f) Thermal cycling stability of MGF@TGO. (g) Infrared images of the MGF and MGF@TGO with increasing heating time.

industrial MGF application in which both function as a thermal management unit. In integrated circuits, the detachment of graphene fragments from MGF during operation may interfere with the normal functioning of the device, potentially leading to issues such as short circuits (Figure 6d). The device details are listed in Figure S18. As shown in Figure 6e, significant amounts of graphene powder remain on the chip in direct contact with MGF, and noticeable scratches are present on the MGF surface. In contrast, MGF@TGO, benefiting from its superior surface stability, remains clean on the chip with no scratches on the surface, retaining its integrity. This result demonstrates that, compared to untreated MGF, MGF@TGO prepared via the SIS strategy exhibits enhanced surface stability under simulated operating conditions, effectively resisting surface wear and nanosheet shedding induced by vibration. Due to the enhanced surface stability provided by the TGO coating, MGF@TGO remains stable after heating at 100 °C for 100 h (Figure S19) and undergoing 300 thermal cycles (Figure 6f). To further evaluate the thermal performance of MGF@TGO under practical conditions, a heat source is placed beneath the sample for simultaneous heating. The infrared images (Figure 6g) demonstrate that MGF@TGO exhibits the same temperature increase rate as MGF, indicating the high retention rate of thermal conductive performance.

CONCLUSIONS

In summary, we develop an interface engineering strategy to address the critical challenge of balancing surface stability and property retention in MGF. The SIS-derived TGO coating, with its unprecedented thickness (5 nm), achieves a record 206.36% adhesion enhancement through synergistic hydrogen bonding and $\pi-\pi$ interactions, while retaining >99% of MGF's electrical conductivity and thermal conductivity. In simulated vibration tests under operating conditions, MGF@TGO demonstrates excellent stability without shedding and remains stable during 300 cycles of thermal stability testing (total time: 900 min). This work resolves the long-standing trade-off between surface stability and performance in MGF, offering a scalable and versatile solution for industrial applications. Our findings not only advance the fundamental understanding of interfacial engineering in 2D material systems but also pave the way for deploying high-performance MGF in next-generation energy storage, electronics, and thermal management technologies.

METHODS

Materials. The MGF with a thickness of 15 μm is purchased from Hanene Technology Co., Ltd. in Wuhan, China. Large-size graphene oxide (GO) powder is purchased from Yicheng Technology Co., Ltd. in Wuxi, China. Triton X-100 and ethyl acetate (EA) are purchased from Macklin Industrial Co., Ltd. Deionized water is obtained in the laboratory.

Fabrication of MGF@GO. First, the GO dispersion is prepared at a concentration of 0.1 mg mL^{-1}. Second, droplets of EA solvent are continuously dropped onto the surface of the diluted GO suspension. Within a few minutes, a large-area GO membrane with a thickness of 5 nm, densely packed in a few-layered structure, is spontaneously assembled at the air−liquid interface along the lateral direction. Third,

https://doi.org/10.1021/acsami.5c05545
ACS Appl. Mater. Interfaces XXXX, XXX, XXX−XXX

the uplifted GO membrane is transferred onto the graphene film and dried at 40 °C for 4 h under a vacuum to remove residual solvent.

Fabrication of MGF@TGO. First, a GO dispersion with a concentration of 5 mg mL^{-1} is prepared. Triton X-100 is then added at 1.5% of the GO mass fraction and stirred thoroughly. Second, the solution is diluted 50 times, and droplets of EA solvent are continuously dropped onto the surface of the diluted TGO suspension. Within a few minutes, a large-area TGO film with a thickness of 5 nm and a dense multilayered structure is spontaneously aggregated at the gas−liquid interface. Third, the uplifted TGO film is transferred onto the graphene film and vacuum-dried at 40 °C for 4 h to remove residual solvent.

Material Characterization. Samples for HRTEM are prepared at −150 °C by cutting with an ion gun to a thickness of less than 100 nm. HRTEM images are collected using a JEOL-F200 equipped with a Cs probe aberration corrector, XMAX 100 EDX detector (Oxford Instruments), high-angle annular dark-field detector, and segmented detectors. The system is operated at 300 kV. The adhesion force of different samples was studied by using atomic force microscopy (AFM, Bruker Dimension Icon). For each sample, 25 points were randomly selected from the measured adhesion mapping to represent the adhesion force. SEM images are captured using a dual-beam electron microscope (Zeiss Crossbeam 350). The X-ray source is Al monochromatic radiation working at 25.0 W with a beam diameter of 100.0 μm. The neutralizer is set at 0.3 V and 5.0 μA, with the analysis mode preferred as the fixed analyzer transmission mode. The C 1s spectrum of carbon and the O 1s spectrum use the same parameters: a pass energy of 112 eV and an energy step of 0.1 eV. Charge (binding energy scale) calibration is performed by using C 1s at 284.8 eV. Fourier transform infrared (FTIR) spectra are recorded on a Nicolet 60-SXB IR instrument in attenuated total reflection mode. Contact angles are measured by static contact angle technology, capturing droplet images with a KRÜSS Scientific DSA30B. The droplet is deionized water, and images are captured after the droplet stabilizes on the sample surface. Contact angles are automatically fitted using an appropriate algorithm. XRD patterns are acquired on a Rigaku SmartLab using Cu Kα radiation (λ = 1.5406 Å) at a scanning speed of 5° min^{-1}. The stress−strain curves of the samples are tested on a universal testing machine (MTS E44.104). Infrared photographs are captured using an infrared camera (DS-2TPH16-6AVF). C K-edge XANES measurements were performed at beamlines BL10B of the NSRL in Hefei, China. The resolving power (E/ΔE) is ≈ 2000, and the photon flux is 5×10^9 photons per second. For the normalization procedure, the pre-edge was set to 0, and the edge jump was normalized to 1. In accordance with the measurement principle of ASTM D5470, a DRL-III60D thermal conductivity tester (Xiangtan Xiangyi Instrument Co., Ltd.) is employed to measure the thermal conductivity of the sample. Each sample was measured three times to calculate the mean value and the corresponding error. MGF@TGO is placed on a slide, a pressure of 50 N is applied, and the slide is slowly moved. The exfoliation of graphene fragments is observed under an optical microscope.

■ ASSOCIATED CONTENT

Supporting Information

The Supporting Information is available free of charge at https://pubs.acs.org/doi/10.1021/acsami.5c05545.

Additional characterizations of samples, including AFM images, SEM images, optical photographs of the fragments, full XPS spectra, simulated operating condition image, etc (PDF)

■ AUTHOR INFORMATION

Corresponding Authors

Bo Liu − *Sanya Science and Education Innovation Park of Wuhan University of Technology, Sanya 572000, China; Hubei Engineering Research Center of RF-Microwave Technology and Application, School of Physics and Mechanics, Wuhan University of Technology, Wuhan 430070, China*; Email: liubo2024@whut.edu.cn

Geng Wu − *School of Materials Science and Engineering, Wuhan University of Technology, Wuhan 430070, China*; Email: gengwu@mail.ustc.edu.cn

Daping He − *Sanya Science and Education Innovation Park of Wuhan University of Technology, Sanya 572000, China; School of Materials Science and Engineering and Hubei Engineering Research Center of RF-Microwave Technology and Application, School of Physics and Mechanics, Wuhan University of Technology, Wuhan 430070, China*; orcid.org/0000-0002-0284-4990; Email: hedaping@whut.edu.cn

Authors

Mingyang Tanwei − *Sanya Science and Education Innovation Park of Wuhan University of Technology, Sanya 572000, China; School of Materials Science and Engineering, Wuhan University of Technology, Wuhan 430070, China*

Zibo Chen − *Sanya Science and Education Innovation Park of Wuhan University of Technology, Sanya 572000, China; School of Materials Science and Engineering, Wuhan University of Technology, Wuhan 430070, China*

Yunfa Si − *Sanya Science and Education Innovation Park of Wuhan University of Technology, Sanya 572000, China; School of Materials Science and Engineering, Wuhan University of Technology, Wuhan 430070, China*

Yongyi Ji − *Sanya Science and Education Innovation Park of Wuhan University of Technology, Sanya 572000, China; School of Materials Science and Engineering, Wuhan University of Technology, Wuhan 430070, China*

Shiya Cao − *School of Materials Science and Engineering, Wuhan University of Technology, Wuhan 430070, China*

Zhenyu Gong − *Sanya Science and Education Innovation Park of Wuhan University of Technology, Sanya 572000, China; School of Materials Science and Engineering, Wuhan University of Technology, Wuhan 430070, China*

Bao-Wen Li − *School of Materials Science and Engineering and State Key Laboratory of Advanced Technology for Materials Synthesis and Processing, Center of Smart Materials and Devices, Wuhan University of Technology, Wuhan 430070, China*; orcid.org/0000-0003-0846-6916

Complete contact information is available at: https://pubs.acs.org/10.1021/acsami.5c05545

Author Contributions

[⊥]M.T. and Z.C. contributed equally to this work.

Notes

The authors declare no competing financial interest.

■ ACKNOWLEDGMENTS

The authors sincerely acknowledge financial support from the National Natural Science Foundation of China (22279097), the Key R&D Program of Hubei Province (2023BAB103), the Foundation of National Key Laboratory of Microwave Imaging Technology, and the PhD Scientific Research and Innovation Foundation of Sanya Yazhou Bay Science and Technology City (No. HSPHDSRF-2023-03-013 and No. HSPHDSRF-2023-03-012). The authors further extend their acknowledgments to the Institutional Center for Shared Technologies and Facilities

of IDSSE, CAS, for the assistance provided by intermediate engineers Dongmei Wang and Shuang Liu. Additionally, the authors would like to thanks beamlines BL10B at NSRL for enabling soft X-ray absorption spectroscopy characterizations via Synchrotron Radiation.

REFERENCES

(1) El-Kady, M. F.; Shao, Y.; Kaner, R. B. Graphene for Batteries, Supercapacitors and Beyond. *Nat. Rev. Mater.* **2016**, *1* (7), 16033.
(2) Li, H.; Lim, J. H.; Lv, Y.; Li, N.; Kang, B.; Lee, J. Y. Graphynes and Graphdiynes for Energy Storage and Catalytic Utilization: Theoretical Insights into Recent Advances. *Chem. Rev.* **2023**, *123* (8), 4795−4854.
(3) Bi, J.; Du, Z.; Sun, J.; Liu, Y.; Wang, K.; Du, H.; Ai, W.; Huang, W. On the Road to the Frontiers of Lithium-Ion Batteries: A Review and Outlook of Graphene Anodes. *Adv. Mater.* **2023**, *35* (16), No. 2210734.
(4) Dai, W.; Wang, Y.; Li, M.; Chen, L.; Yan, Q.; Yu, J.; Jiang, N.; Lin, C. 2D Materials-Based Thermal Interface Materials: Structure, Properties, and Applications. *Adv. Mater.* **2024**, *36* (37), No. 2311335.
(5) Chen, X.; Cheng, P.; Tang, Z.; Xu, X.; Gao, H.; Wang, G. Carbon-Based Composite Phase Change Materials for Thermal Energy Storage, Transfer, and Conversion. *Adv. Sci.* **2021**, *8* (9), No. 2001274.
(6) Feng, C.-P.; Wei, F.; Sun, K.-Y.; Wang, Y.; Lan, H.-B.; Shang, H.-J.; Ding, F.-Z.; Bai, L.; Yang, J.; Yang, W. Emerging Flexible Thermally Conductive Films: Mechanism, Fabrication, Application. *Nano-Micro Lett.* **2022**, *14* (1), 127.
(7) Lee, J.; Cho, K.; Kim, J. Age of Flexible Electronics: Emerging Trends in Soft Multifunctional Sensors. *Adv. Mater.* **2024**, *36* (16), No. 2310505.
(8) Jiang, S.; Liu, X.; Liu, J.; Ye, D.; Duan, Y.; Li, K.; Yin, Z.; Huang, Y. Flexible Metamaterial Electronics. *Adv. Mater.* **2022**, *34* (52), No. 2200070.
(9) Xue, J.; Liu, D.; Li, D.; Hong, T.; Li, C.; Zhu, Z.; Sun, Y.; Gao, X.; Guo, L.; Shen, X.; Ma, P.; Zheng, Q. New Carbon Materials for Multifunctional Soft Electronics. *Adv. Mater.* **2025**, *37* (2), No. 2312596.
(10) Lin, Z.; Huang, Y.; Duan, X. Van Der Waals Thin-Film Electronics. *Nat. Electron.* **2019**, *2* (9), 378−388.
(11) Li, L.; Yang, J.; Tan, R.; Shu, W.; Low, C. J.; Zhang, Z.; Zhao, Y.; Li, C.; Zhang, Y.; Li, X.; Zhang, H.; Zhao, X.; Kou, Z.; Xiao, Y.; Verpoort, F.; Wang, H.; Mai, L.; He, D. Large-Scale Current Collectors for Regulating Heat Transfer and Enhancing Battery Safety. *Nat. Chem. Eng.* **2024**, *1* (8), 542−551.
(12) Lee, G.; Jang, S.; Kim, Y.; Cho, D.; Jeong, D.; Chae, S.; Myoung, J.; Kim, H.; Kim, S.; Lee, J. Ultrathin Metal Film on Graphene for Percolation-Threshold-Limited Thermal Emissivity Control. *Adv. Mater.* **2023**, *35* (38), No. 2301227.
(13) Akbari, A.; Cunning, B. V.; Joshi, S. R.; Wang, C.; Camacho-Mojica, D. C.; Chatterjee, S.; Modepalli, V.; Cahoon, C.; Bielawski, C. W.; Bakharev, P.; Kim, G.-H.; Ruoff, R. S. Highly Ordered and Dense Thermally Conductive Graphitic Films from a Graphene Oxide/Reduced Graphene Oxide Mixture. *Matter* **2020**, *2* (5), 1198−1206.
(14) Xin, G.; Sun, H.; Hu, T.; Fard, H. R.; Sun, X.; Koratkar, N.; Borca-Tasciuc, T.; Lian, J. Large-Area Freestanding Graphene Paper for Superior Thermal Management. *Adv. Mater.* **2014**, *26* (26), 4521−4526.
(15) Peng, L.; Xu, Z.; Liu, Z.; Guo, Y.; Li, P.; Gao, C. Ultrahigh Thermal Conductive yet Superflexible Graphene Films. *Adv. Mater.* **2017**, *29* (27), No. 1700589.
(16) Novoselov, K. S.; Geim, A. K.; Morozov, S. V.; Jiang, D.; Zhang, Y.; Dubonos, S. V.; Grigorieva, I. V.; Firsov, A. A. Electric Field Effect in Atomically Thin Carbon Films. *Science* **2004**, *306* (5696), 666−669.
(17) Nyholm, N.; Espallargas, N. Functionalized Carbon Nanostructures as Lubricant Additives − A Review. *Carbon* **2023**, *201*, 1200−1228.
(18) Berman, D.; Erdemir, A.; Sumant, A. V. Graphene: A New Emerging Lubricant. *Mater. Today* **2014**, *17* (1), 31−42.
(19) Xu, L.; Ma, T.; Hu, Y.; Wang, H. Molecular Dynamics Simulation of the Interlayer Sliding Behavior in Few-Layer Graphene. *Carbon* **2012**, *50* (3), 1025−1032.
(20) Wang, C.; Gao, B.; Fang, F.; Qi, W.; Yan, G.; Zhao, J.; Wang, W.; Bai, R.; Zhang, Z.; Zhang, Z.; Zhang, W.; Yan, X. A Stretchable and Tough Graphene Film Enabled by Mechanical Bond. *Angew. Chem., Int. Ed.* **2024**, *63* (28), No. e202404481.
(21) Wan, S.; Chen, Y.; Fang, S.; Wang, S.; Xu, Z.; Jiang, L.; Baughman, R. H.; Cheng, Q. High-Strength Scalable Graphene Sheets by Freezing Stretch-Induced Alignment. *Nat. Mater.* **2021**, *20* (5), 624−631.
(22) Wen, Y.; Wu, M.; Zhang, M.; Li, C.; Shi, G. Topological Design of Ultra-strong and Highly Conductive Graphene Films. *Adv. Mater.* **2017**, *29* (41), No. 1702831.
(23) Hao, Y.; Ming, X.; Lu, J.; Cao, M.; Zhang, P.; Shi, H.; Li, K.; Gao, Y.; Wang, L.; Fang, W.; Chen, Y.; Zhang, L.; Sun, H.; Gao, W.; Liu, Y.; Xu, Z.; Gao, C. Bidirectionally High-Thermally Conductive and Environmentally Adaptive Graphene Thick Films Enabled by Seamless Bonding Assembly for Extreme Thermal Management. *Adv. Funct. Mater.* **2024**, *34* (29), No. 2400110.
(24) Huang, Y.; Su, Y.; Guo, X.; Guo, Q.; Ouyang, Q.; Zhang, G.; Zhang, D. Fabrication and Thermal Conductivity of Copper Coated Graphite Film/Aluminum Composites for Effective Thermal Management. *J. Alloys Compd.* **2017**, *711*, 22−30.
(25) Wang, X.; Su, Y.; Ouyang, Q.; Zhu, C.; Cao, H.; Zhang, D. Fabrication, Mechanical and Thermal Properties of Copper Coated Graphite Films Reinforced Copper Matrix Laminated Composites via Ultrasonic-Assisted Electroless Plating and Vacuum Hot-Pressing Sintering. *Mater. Sci. Eng., A* **2021**, *824*, No. 141768.
(26) Zhang, P.; Hao, Y.; Shi, H.; Lu, J.; Liu, Y.; Ming, X.; Wang, Y.; Fang, W.; Xia, Y.; Chen, Y.; Li, P.; Wang, Z.; Su, Q.; Lv, W.; Zhou, J.; Zhang, Y.; Lai, H.; Gao, W.; Xu, Z.; Gao, C. Highly Thermally Conductive and Structurally Ultra-Stable Graphitic Films with Seamless Heterointerfaces for Extreme Thermal Management. *Nano-Micro Lett.* **2024**, *16* (1), 58.
(27) Lee, S.; Broido, D.; Esfarjani, K.; Chen, G. Hydrodynamic Phonon Transport in Suspended Graphene. *Nat. Commun.* **2015**, *6* (1), 6290.
(28) Prehal, C.; Freunberger, S. A. Li-O2 Cell-Scale Energy Densities. *Joule* **2019**, *3* (2), 321−323.
(29) Liu, Z.; Ma, Z.; Qian, B.; Chan, A. Y. H.; Wang, X.; Liu, Y.; Xin, J. H. A Facile and Scalable Method of Fabrication of Large-Area Ultrathin Graphene Oxide Nanofiltration Membrane. *ACS Nano* **2021**, *15* (9), 15294−15305.
(30) Soler-Crespo, R. A.; Mao, L.; Wen, J.; Nguyen, H. T.; Zhang, X.; Wei, X.; Huang, J.; Nguyen, S. T.; Espinosa, H. D. Atomically Thin Polymer Layer Enhances Toughness of Graphene Oxide Monolayers. *Matter* **2019**, *1* (2), 369−388.
(31) Ding, G.; Yang, B.; Chen, K.; Wang, H.; Chen, J.; Mei, Q. Enhanced Self−Assembly and Spontaneous Separation for Ultrathin, Air−Floating Graphene Macrofilms and Their Application in Ultrasensitive In-Site Growth Sensors. *Adv. Mater.* **2024**, *36*, No. 2408550.
(32) Jeon, I.; Peeks, M. D.; Savagatrup, S.; Zeininger, L.; Chang, S.; Thomas, G.; Wang, W.; Swager, T. M. Janus Graphene: Scalable Self-Assembly and Solution-Phase Orthogonal Functionalization. *Adv. Mater.* **2019**, *31* (21), No. 1900438.
(33) Zhou, F.; Dong, Q.; Chen, J.-T.; Sengupta, B.; Jiang, J.; Xu, W. L.; Li, H.; Li, S.; Yu, M. Printed Graphene Oxide-Based Membranes for Gas Separation and Carbon Capture. *Chem. Eng. J.* **2022**, *430*, No. 132942.
(34) Hui, F.; Zhang, C.; Yu, H.; Han, T.; Weber, J.; Shen, Y.; Xiao, Y.; Li, X.; Zhang, Z.; Liu, P. Self-Assembly of Janus Graphene Oxide

https://doi.org/10.1021/acsami.5c05545
ACS Appl. Mater. Interfaces XXXX, XXX, XXX−XXX

via Chemical Breakdown for Scalable High-Performance Memristors. *Adv. Funct. Mater.* **2024**, *34*, 15.
(35) Jang, J.; Jung, H. J.; Chong, S.; Kim, D.; Kim, J.; Kim, S. O.; Kim, I. 2D Materials Decorated with Ultrathin and Porous Graphene Oxide for High Stability and Selective Surface Activity. *Adv. Mater.* **2020**, *32* (36), No. 2002723.
(36) Liu, H.; Xu, Z.; Cao, B.; Xin, Z.; Lai, H.; Gao, S.; Xu, B.; Yang, J.-L.; Xiao, T.; Fan, H. J. Marangoni-Driven Self-Assembly MXene As Functional Membrane Enables Dendrite-Free and Flexible Zinc-Iodine Pouch Cells. *Adv. Energy Mater.* **2024**, *14* (26), No. 2400318.
(37) Shim, J.; Yun, J. M.; Yun, T.; Kim, P.; Lee, K. E.; Lee, W. J.; Ryoo, R.; Pine, D. J.; Yi, G.-R.; Kim, S. O. Two-Minute Assembly of Pristine Large-Area Graphene Based Films. *Nano Lett.* **2014**, *14* (3), 1388−1393.
(38) Zhao, T.; Xie, P.; Wan, H.; Ding, T.; Liu, M.; Xie, J.; Li, E.; Chen, X.; Wang, T.; Zhang, Q.; Wei, Y.; Gong, Y.; Wen, Q.; Hu, M.; Qiu, C.-W.; Xiao, X. Ultrathin MXene Assemblies Approach the Intrinsic Absorption Limit in the 0.5−10 THz Band. *Nat. Photonics* **2023**, *17* (7), 622−628.
(39) Ji, X.; Zhao, X.; Zhang, Z.; Si, Y.; Qian, W.; Fu, H.; Chen, Z.; Wang, Z.; Jin, H.; Yang, Z.; He, D. Scalable Fabrication of Graphene-Assembled Multifunctional Electrode with Efficient Electrochemical Detection of Dopamine and Glucose. *Nano Res.* **2023**, *16* (5), 6361−6368.
(40) Cançado, L. G.; Takai, K.; Enoki, T.; Endo, M.; Kim, Y. A.; Mizusaki, H.; Jorio, A.; Coelho, L. N.; Magalhães-Paniago, R.; Pimenta, M. A. General Equation for the Determination of the Crystallite Size La of Nanographite by Raman Spectroscopy. *Appl. Phys. Lett.* **2006**, *88* (16), 163106.
(41) Zhang, L.; Ji, L.; Glans, P.-A.; Zhang, Y.; Zhu, J.; Guo, J. Electronic Structure and Chemical Bonding of a Graphene Oxide-Sulfur Nanocomposite for Use in Superior Performance Lithium-Sulfur Cells. *Phys. Chem. Chem. Phys.* **2012**, *14* (39), 13670.
(42) Ye, Y.; Kawase, A.; Song, M.-K.; Feng, B.; Liu, Y.-S.; Marcus, M. A.; Feng, J.; Fang, H.; Cairns, E. J.; Zhu, J.; Guo, J. X-Ray Absorption Spectroscopic Characterization of the Synthesis Process: Revealing the Interactions in Cetyltrimethylammonium Bromide-Modified Sulfur-Graphene Oxide Nanocomposites. *J. Phys. Chem. C* **2016**, *120* (19), 10111−10117.

https://doi.org/10.1021/acsami.5c05545
ACS Appl. Mater. Interfaces XXXX, XXX, XXX−XXX